

Modeling X-ray reflection spectra from returning radiation: application to 4U 1630–47

Kostas Kourmpetis^{1,2}, Shafqat Riaz², Honghui Liu¹, Temurbek Mirzaev³, Cosimo Bambi^{3,4}, Debroy Das³, Jiachen Jiang⁵, Kostas D. Kokkotas², and Andrea Santangelo¹

¹ Institut für Astronomie und Astrophysik, Eberhard-Karls Universität Tübingen, Sand 1, 72076 Tübingen, Germany

² Theoretical Astrophysics, IAAT, Eberhard-Karls Universität Tübingen, D-72076 Tübingen, Germany

³ Center for Astronomy and Astrophysics, Center for Field Theory and Particle Physics and Department of Physics, Fudan University, 200438 Shanghai, China

⁴ School of Natural Sciences and Humanities, New Uzbekistan University, Tashkent 100007, Uzbekistan

⁵ Department of Physics, University of Warwick, Coventry CV4 7AL, UK

e-mail: kostantinos.kourmpetis@student.uni-tuebingen.de, honghui.liu@uni-tuebingen.de

January 22, 2026

ABSTRACT

Returning radiation is thought to play a key role in disk illumination of black hole X-ray binaries in the high-soft state, yet it has not been fully incorporated into XSPEC reflection models. We present a new table model for reflection spectroscopy that, for the first time, self-consistently accounts for the returning radiation. To isolate this effect, we adopt the standard disk-corona configuration but disable the corona, allowing the reflection spectrum to be produced solely by self-irradiation of the disk. Applying our model to the black hole X-ray binary 4U 1630–47, we report a rapidly spinning black hole ($a_* \sim 0.99$), a disk inclination of $i \sim 53^\circ$, a mass accretion rate of $\dot{M}_{\text{BH}} \sim 15\% M_{\text{Edd}}$, and an electron density of $n_e \sim 10^{21} \text{ cm}^{-3}$ to reproduce the observed reflection features. The model also yields a source distance of $D \sim 8.2 \text{ kpc}$, slightly below the commonly adopted value of 10 kpc in the literature. Compared to the widely used `relxill11NS`, our model naturally produces a harder high-energy reflection spectrum, fitting the data without invoking a Comptonized component.

Key words. X-rays: binaries, Black hole physics, Accretion

1. Introduction

In black hole X-ray binary (XRB) systems, a companion star transfers matter onto a stellar-mass black hole, forming an accretion disk that emits strongly in X-rays (Shakura & Sunyaev 1973; Novikov & Thorne 1973). Determining the spin of stellar-mass black holes is crucial, as it provides insight into the collapse of massive stars and may help explain high-energy phenomena such as relativistic jets (e.g., Penrose 1969; Blandford & Znajek 1977; King & Kolb 1999; Miller & Miller 2015). Several techniques have been developed to measure spins, including the continuum-fitting method (Zhang et al. 1997; McClintock et al. 2014), X-ray reflection spectroscopy (Fabian et al. 1989; Reynolds 2014; Bambi et al. 2021), quasi-periodic oscillations (Motta et al. 2014a,b; Ingram & Motta 2019; Liu et al. 2021) and gravitational-wave detections (Abbott et al. 2016; Abbott et al. 2019). Among these, reflection spectroscopy stands out as a particularly powerful diagnostic tool, as it probes the innermost regions of accreting systems (e.g., Fabian et al. 2012; García et al. 2015; Walton et al. 2016; Liu et al. 2023a,b) and enables tests of General Relativity in the strong-field regime (De Rosa et al. 2019; Reynolds 2021; Bambi et al. 2021; Tripathi et al. 2021b, 2019; Liu et al. 2019, 2020).

As shown in Fig. 1(a), the observed spectrum of black hole XRBs typically consists of three primary components: (i) a thermal component originating from a geometrically thin, optically thick accretion disk¹ (Shakura & Sunyaev 1973; Page & Thorne 1974) ; (ii) a Comptonized component produced by a hot corona² that inverse-Compton scatters soft disk photons (Thorne & Price 1975; Shapiro et al. 1976) ; and (iii) a reflection component resulting from the illumination of the disk by the corona (George & Fabian 1991). The disk is thought to be cold as it can efficiently emit radiation and its thermal spectrum peaks in the soft X-rays ($\sim 1 \text{ keV}$). The coronal spectrum takes a power-law-like form that can extend to above 100 keV.

In the rest frame of the accretion disk material, the reflected X-ray spectrum typically features narrow fluorescent emission lines at lower energies and a pronounced Compton hump peaking between 20 and 40 keV (Ross & Fabian 2005;

¹ An accretion disk is considered geometrically thin when $h/r \ll 1$, where h is the disk scale height at radius r , and optically thick if $h \gg \lambda$, with λ denoting the photon mean free path.

² The corona is some hot plasma ($\sim 100 \text{ keV}$) in the region surrounding the black hole and its precise geometry remains uncertain (see, e.g., Bambi 2017; Li et al. 2025, for a discussion and evaluation of different geometries).

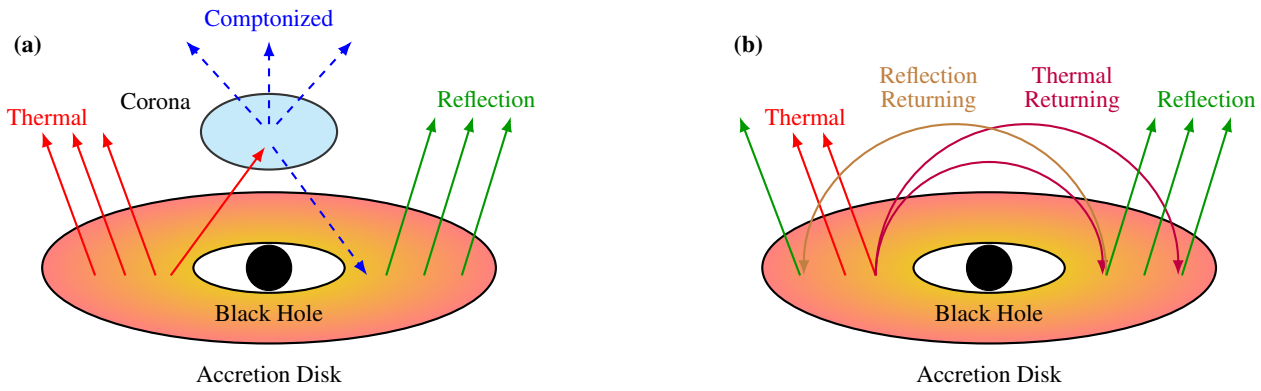


Fig. 1. Schematic illustration of (a) a black hole-disk-corona model including thermal, Compton, and reflection components, and (b) a black hole-disk model with reflection component from self-irradiation of the disk (thermal returning) and iterative reflection (reflection returning). The color gradient in the disk indicates that the temperature increases towards the black hole.

(Garcia & Kallman 2010). The most notable spectral line is generally the iron $K\alpha$ complex, which appears at 6.4 keV for neutral or weakly ionized iron, and shifts up to 6.97 keV for fully ionized, hydrogen-like iron³. However, when observed from a distant point, the disk's entire reflection spectrum appears smeared due to relativistic effects (Fabian et al. 1989; Laor 1991; Fabian et al. 2000; Dauser et al. 2010).

X-ray reflection spectroscopy has advanced significantly in recent years. The current state-of-the-art is represented by relativistic models such as `relxill`⁴ (Dauser et al. 2013; Garcia et al. 2014), `reltrans`⁵ (Ingram et al. 2019), `reflkerr` (Niedzwiecki & Zycki 2008; Niedzwiecki et al. 2019), and `kyn`⁶ (Dovciak et al. 2004), as well as radiative transfer models like `xillver` (Garcia et al. 2013) and `reflionx`⁷ (Ross & Fabian 2005), which compute the reflection spectra in the rest frame of the material of the disk.

While these frameworks represent major improvements over earlier generations, they still rely on simplifying assumptions concerning the disk structure, coronal geometry, and the treatment of relativistic effects (e.g., Bambi et al. 2021; Liu et al. 2025; Huang et al. 2025). Some simplifications are relatively benign. For example, the assumption of infinitesimally thin, Keplerian disks often provides accurate results for rapidly rotating sources (Shashank et al. 2022; Abdikamalov et al. 2020; Tripathi et al. 2020, 2021a; Jiang et al. 2022). However, such simplifications can introduce substantial systematic uncertainties if applied to systems near the Eddington accretion limit, since the disk becomes progressively thicker and therefore cannot be described via the thin-disk model (Riaz et al. 2020a,b).

A particularly important effect in this context is *returning radiation* (or self-irradiation) (purple and brown arrows in Fig. 1(b)), i.e., disk emission that is bent back onto the accretion disk by the strong gravitational field of the black hole. The first calculations of this effect were performed by Cunningham (1976) in the context of thermal disk spectra, while Li et al. (2005) later showed that it can mimic the effect of a higher accretion rate. Although usually neglected in thermal spectral fitting,

returning radiation has been shown to significantly influence polarization signatures (Schnittman & Krolik 2009).

The role of returning radiation in reflection spectra was first examined in Dabrowski et al. (1997), who concluded it is negligible if the corona corotates with the disk. Niedzwiecki & Zycki (2008) confirmed this but showed that the effect becomes important for a static corona close to the black hole. Subsequent studies in the lamppost geometry (Niedzwiecki et al. 2016; Niedzwiecki & Zdziarski 2018) demonstrated that returning radiation can significantly alter the reflection spectrum under certain conditions. More recent work, employing a range of approximations, has further investigated this effect (Wilkins et al. 2020; Dauser et al. 2022; Riaz et al. 2021, 2023). These studies generally agree that returning radiation is especially relevant for rapidly spinning black holes ($a_* \geq 0.9$) with compact coronae illuminating the innermost disk (e.g., lamppost heights $h < 5 r_g$, where r_g is the gravitational radius).

Different approaches have been proposed to incorporate returning radiation in reflection modeling. For instance, Dauser et al. (2022) introduced a modified emissivity profile within `relxill`, though still assuming the illuminating flux follows a simple cutoff power law in the disk rest frame. However, because the spectrum of returning radiation itself has the form of a reflection spectrum rather than a power law, its effect cannot always be absorbed into emissivity modifications (Mirzaev et al. 2024b). In fact, for systems where the disk extends very close to the event horizon, the corona predominantly illuminates the innermost disk, and the ionization parameter is low to moderate, returning radiation can substantially reshape the reflection spectrum. In such cases, computing the rest-frame reflection spectrum at each disk radius using the true incident spectrum, a mix of coronal power law and reflected, becomes essential. Otherwise, spectral fits may fail, leading to significantly biased parameter estimates (Mirzaev et al. 2024b).

This work is motivated by two key considerations. First, despite its potential importance, returning radiation has received little attention in scenarios where the corona is weak or absent, as is often the case in the soft state. Second, there is currently no XSPEC model that self-consistently accounts for returning radiation. In the high-soft state, self-irradiation of the disk is expected to dominate and may reveal novel observational signatures in the reflection spectrum. The primary aim of this study is therefore to construct a table model that captures the effect of returning radiation on disk reflection in a pure-disk scenario,

³ As the ionization increases, reduced electron shielding results in a higher effective nuclear charge, shifting the line energy upwards.

⁴ <https://www.sternwarte.uni-erlangen.de/~dauser/research/relxill/>

⁵ <https://github.com/reltrans/reltrans>

⁶ <https://projects.asu.cas.cz/stronggravity/kyn>

⁷ https://github.com/honghui-liu/reflionx_tables

and to test its performance by fitting real observational data of sources in the soft state.

This paper is structured as follows: in Section 2, we describe the details of the physical model and the code utilized, alongside its implementation in XSPEC to generate the corresponding table model. Section 3 presents the spectral analysis of 4U 1630–47 using both our model and the widely used `relxillNS`, including the fitting procedure and interpretation of the results. Finally, Section 4 summarizes the main conclusions of this work and outlines possible directions for future studies. Throughout the analysis, we adopt the $u_\mu u^\mu = -1$ convention for timelike four-velocities, we use Boyer-Lindquist coordinates for the Kerr metric and employ natural units ($c = G = \hbar = k_B = 1$), unless stated otherwise.

2. Model Development

2.1. The `ziji` code

We focus on modeling the reflection spectrum in the absence of any coronal emission. We adapt an updated, unpublished version of the `ziji` code (the original code is available on GitHub⁸), presented in Mirzaev et al. (2024a), and disable the corona by setting its luminosity to zero, thereby isolating the effect of returning radiation on the reflection spectrum.

The default spacetime metric in our model is the Kerr solution (Kerr 1963). However, `ziji` does not rely on any specific equation or property of the Kerr metric, allowing us to adopt any stationary, axisymmetric, and asymptotically flat spacetime by simply modifying the metric coefficients (Mirzaev et al. 2024a).

The accretion disk is described by the Novikov-Thorne disk (Page & Thorne 1974; Novikov & Thorne 1973). The disk is assumed to be infinitesimally thin and oriented perpendicular to the black hole's spin axis, with its inner edge located at the innermost stable circular orbit (R_{isco}), while its back-reaction to the spacetime metric is negligible (Page & Thorne 1974; Bambi 2024b). Material within the disk follows nearly geodesic, equatorial and circular trajectories. The time-averaged energy flux from the disk at radius r is (Page & Thorne 1974; Bambi 2017):

$$F(r) = \frac{\dot{M}_{\text{BH}}}{4\pi M_{\text{BH}}^2} \mathcal{F}(r), \quad (1)$$

where \dot{M}_{BH} is the mass accretion rate and M_{BH} is the black hole mass. $\mathcal{F}(r)$ is a dimensionless function dependent on the specific angular momentum L_z , energy E , and angular velocity Ω of the orbiting gas (Bambi 2024a):

$$\mathcal{F}(r) = -\frac{\partial_r \Omega}{(E - \Omega L_z)^2} \frac{M_{\text{BH}}^2}{\sqrt{-G}} \int_{r_{\text{in}}}^r (E - \Omega L_z) (\partial_\rho L_z) d\rho, \quad (2)$$

where (see, e.g., Bambi 2017):

$$\Omega = \frac{-\partial_r g_{t\phi} \pm \sqrt{(\partial_r g_{t\phi})^2 - (\partial_r g_{tt})(\partial_r g_{\phi\phi})}}{\partial_r g_{\phi\phi}}, \quad (3)$$

$$E = -\frac{g_{tt} + \Omega g_{t\phi}}{\sqrt{-g_{tt} - 2\Omega g_{t\phi} - \Omega^2 g_{\phi\phi}}}, \quad (4)$$

$$L_z = \frac{g_{t\phi} + \Omega g_{\phi\phi}}{\sqrt{-g_{tt} - 2\Omega g_{t\phi} - \Omega^2 g_{\phi\phi}}}. \quad (5)$$

Here, G is the determinant of the near equatorial plane metric and r_{in} is the inner edge radius of the accretion disk ($r_{\text{in}} \geq R_{\text{isco}}$).

⁸ <https://github.com/ABHModels/ziji/>

In the expression of Ω the $+$ sign is for corotating orbits and the $-$ sign is for counterrotating orbits.

The disk's effective temperature is derived via the Stefan-Boltzmann law, $F = \sigma T_{\text{eff}}^4$, and corrected for non-thermal effects using a hardening (or color) factor f_{col} :

$$T_{\text{col}} = f_{\text{col}} T_{\text{eff}}. \quad (6)$$

The specific intensity of the radiation in the rest-frame of the material in the disk is (Bambi 2024a):

$$I = \frac{2h\nu_e^3}{c^2} \frac{1}{f_{\text{col}}^4} \frac{\Upsilon}{e^{\frac{h\nu_e}{k_B T_{\text{col}}}} - 1}, \quad (7)$$

where ν_e is the frequency of the emitted photons, h is Planck's constant, c is the speed of light, k_B is the Boltzmann constant, and $\Upsilon = \Upsilon(\vartheta_e)$ is a function that accounts for the angular dependence of the emission. In the Kerr spacetime, the thermal emission at each radius is determined by the black hole mass M_{BH} , mass accretion rate \dot{M}_{BH} , spin a_* , color-correction factor f_{col} (fixed at 1.7 in the entire analysis), and the angular factor Υ (set to 1 for isotropic emission), as also noted in Mirzaev et al. (2024a). The `ziji` code also treats iron abundance as a free parameter. Throughout all subsequent modeling, the iron abundance is fixed to the solar value ($A_{\text{Fe}} = 1$).

The ionization ξ at each radius r is given by:

$$\xi(r) = \frac{4\pi\Phi_X(r)}{n_e(r)}, \quad (8)$$

where $\Phi_X(r)$ is the incident flux from returning radiation and $n_e(r)$ is the electron number density, assumed to be constant in this work.

The luminosity of the accretion disk is:

$$L_{\text{disk}} = \eta \dot{M}_{\text{BH}} c^2, \quad (9)$$

where $\eta = 1 - E_{r_{\text{in}}}$ is the efficiency of the system and $E_{r_{\text{in}}}$ is the conserved specific energy calculated at the radius of the inner edge of the disk r_{in} (Bambi 2017). We note that we modified the `ziji` code to accept the mass accretion rate as an input parameter instead of the luminosity (using Eq. 9), as our primary interest lies in exploring variations in M_{BH} .

To compute the reflection spectrum in the rest frame of the disk, we use the `reflionx` code⁹ (Ross & Fabian 2005). The radiation field incident on any point on the disk in our model includes only:

- returning thermal radiation (purple arrows in Fig. 1(b); 0th iteration),
- higher-order returning reflection radiation up to 3 iterations¹⁰ (brown arrow in Fig. 1(b); 1st iteration).

Finally, once the spectra in the rest frame of the disk in every radial bin is calculated, the relativistic spectra as seen by a distant

⁹ We employ the `reflionx` code rather than the `reflionx` table, since the latter one assumes that the disk is illuminated by a power law spectrum with a high-energy cutoff (Mirzaev et al. 2024b).

¹⁰ To avoid confusion, we note that in the papers where the `ziji` code was presented (Mirzaev et al. 2024a,b), up to 4 iterations were performed. The 0th iteration corresponds to the reflection component produced by the corona. In our case, there is no corona; therefore, we perform one fewer iteration (0–3). Physically, the procedure is identical.

observer is computed via ray-tracing. The observed spectral flux is given by (Bambi 2024a):

$$F_o(E_o) = \int_{\text{source}} I_o(E_o, X, Y) d\Omega \quad (10)$$

$$= \frac{1}{D^2} \int_{\text{source}} g^3 I_e(E_e, r_e, \theta_e) dX dY, \quad (11)$$

where the subscripts o and e stand for observed and emitted respectively. D is the distance between the observer and the source, $g = E_o/E_e$ is the redshift factor and $I_o = g^3 I_e$, following from the Liouville's theorem (see Lindquist 1966, for more details). X and Y are the the Cartesian coordinates in the plane of the distant observer and $d\Omega = dXdY/D^2$ the respective infinitesimal solid angle. Lastly, r_e denotes the radius at which the photon is emitted in the accretion disk, while θ_e represents the emission angle measured in the rest frame of the disk material (see discussion in Section 3.3). For a detailed description of ray-tracing, we refer to Bambi (2024a), section VI.

2.2. XSPEC Table Model(s) Generation

To construct the XSPEC table model, we compute the blackbody and reflection spectra over a grid of parameters, as listed in Table 1. Our table model includes 5 parameters:

1. electron density (n_e),
2. dimensionless spin parameter (a_*),
3. black hole mass (M_{BH}),
4. mass accretion rate (\dot{M}_{BH}),
5. inclination angle (i).

The physical distance of the source is absorbed inside the normalization of the model, which is automatically introduced by XSPEC (see Appendix B).

As an initial step, we calculate the spectra in the rest frame of the disk, since including the inclination angle in the full grid would substantially increase the computational time because the code performs ray-tracing in all iterations and we are interested only in the last one. Once the rest-frame spectra are calculated, we perform ray-tracing for the 3rd iteration only, in order to obtain the spectra in the observer's rest frame.

The full grid contains 9,100 points and was chosen based on parameter values commonly reported in the literature for the X-ray binary 4U 1630–47 during the high-soft state, which serves as the test case for our model (see Section 3). The electron density (n_e) spans from 10^{18} to 10^{22} cm^{-3} ; lower densities would yield high ionization parameters (see Eq. 8), significantly weakening the reflection features. This is illustrated in Fig. 2(c) where even for $n_e = 10^{19} \text{ cm}^{-3}$ the reflection features are nearly absent¹¹. The mass accretion rate (\dot{M}_{BH}) covers a range of $(0.14 - 2.1) 10^{18} \text{ g/s}$. For reference, for a maximally spinning $10 M_{\odot}$ black hole, a mass accretion rate of $1.4 \cdot 10^{18} \text{ g/s}$ corresponds to approximately 30% of the Eddington accretion rate ($\dot{M}_{\text{Edd}} = L_{\text{Edd}}/\eta c^2$). This value is typically taken as the upper limit of validity of the thin-disk approximation, as higher accretion rates lead to geometrically thick disks that are no longer well described by the Novikov-Thorne model (Riaz et al. 2020a,b). The black hole spin parameter (a_*) ranges from approximately

0.8 up to the Thorne limit (0.9982), while the mass (M_{BH}) is fixed to $10 M_{\odot}$. Lastly, the inclination angle (i) is permitted to vary between 30° and 75° .

The effect of each of the model's parameters on the spectra is illustrated in Fig. 2, where the black body and reflection (3rd iteration) spectra are plotted for different values of the spin (a), mass accretion rate (b), electron density (c), and inclination angle (d). In each panel, we vary one parameter while the others remain fixed. The parameter values are chosen simply to demonstrate the qualitative behaviour of the model.

The spin significantly shapes the reflection spectra, as shown in Fig. 2(a). Furthermore, in Fig. 3, we present the returning radiation flux profile in the rest frame of the disk for a $10 M_{\odot}$ black hole at different spin values. An increase in spin leads to higher flux returning to each radial bin of the disk, in agreement with the enhanced flux observed at higher spins in Fig. 2(a), because R_{isco} moves closer to the black hole. Fig. 2(b) shows that increasing the mass accretion rate primarily raises the overall flux without significantly affecting the reflection features, while panel (d) illustrates that higher inclinations shift the spectrum to high energies and "wash-out" the emission lines in the soft X-rays due to stronger relativistic effects. The effect of varying the electron density, shown in panel (c), was discussed earlier. The reflection spectra in all panels share a common feature: in the absence of a corona, the Compton hump is weak or even absent, which might be a signature of sources in the high-soft state. A similar result was also reported in previous studies (see, e.g., Mirzaev et al. 2024a; Connors et al. 2021).

Finally, we generate two separate additive XSPEC table models for the relativistic spectra: one for the thermal emission (`zijiBB`) and one for the reflection component (`zijiRef1`). By combining these two files, we constructed a single model that incorporates both the reflection and blackbody components, namely `zijiRetRad`.

3. Spectral Analysis of 4U 1630–47

We proceed by testing our custom table models on the black hole XRB 4U 1630–47, using a *NuSTAR* observation (Obs. ID 80802313002) with an exposure time of 16.2 ksec, taken while the source was in the soft state (see Fig. 2 in Das et al. 2025). We select 4U 1630–47, as Connors et al. (2021) have shown that in the soft state, returning radiation likely dominates disk illumination.

The *NuSTAR* data were processed using NuSTAR-DAS v2.1.1 along with the *NuSTAR* CALDB v20230307. Cleaned event files for both FPMA and FPMB were produced using the `nupipeline` tool. Source spectra were extracted from a circular aperture of $150''$ radius centered on the source, while background spectra were taken from a source-free circular aperture of $180''$ radius. The spectra and associated data products were generated via the `nuproducts` tool. The FPMA and FPMB spectra are grouped to have a minimum count of 30 photons per bin. Spectral fitting was performed with XSPEC v12.15.0 (Arnaud 1996), using χ^2 statistics to determine the best-fit values and parameter uncertainties.

3.1. Model Setup

To motivate the model construction using `zijiRetRad`, we present the process step by step, justifying the inclusion of each component. We fix the black hole mass to $10 M_{\odot}$ (Seifina et al. 2014, indirect mass estimate) and begin with the baseline model (in XSPEC language):

¹¹ At high ionization parameters the disk surface becomes highly ionized, reducing photoelectric opacity and suppressing fluorescent line production. As a result, characteristic reflection features, particularly the Fe $K\alpha$ line and absorption edges, are weakened and the spectrum becomes dominated by a smooth Compton-scattered continuum.

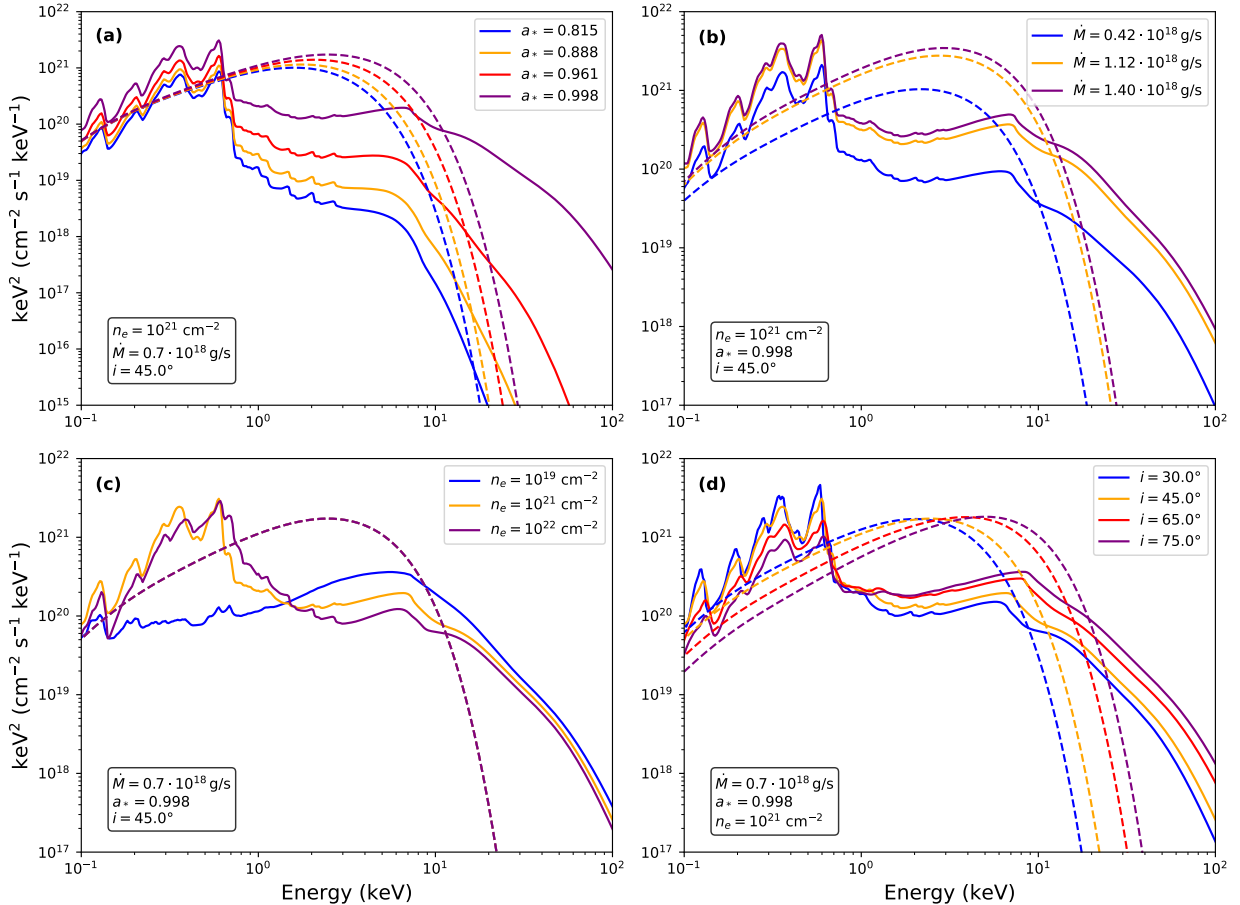


Fig. 2. Reflection spectra (solid lines) produced by returning radiation (3rd iteration) and black-body spectra (dashed lines) from the `ziji` code for a $10 M_{\odot}$ black hole, showing the impact of spin (a), mass accretion rate (b), electron density (c), and inclination angle (d) on the spectra.

Model Parameter	Values
Electron density: n_e (cm^{-3})	$10^{18}, 10^{19}, 10^{20}, 10^{21}, 10^{22}$
Spin parameter: a_*	0.8146, 0.8346, 0.8534, 0.8710, 0.8876, 0.9035, 0.9187, 0.9332, 0.9471, 0.9605, 0.9735, 0.9861, 0.9982
Black hole mass: M_{BH} (M_{\odot})	10
Mass accretion rate: \dot{M}_{BH} (10^{18} g/s)	0.14, 0.42, 0.70, 0.84, 0.98, 1.12, 1.26, 1.40, 1.68, 2.1
Inclination angle: i ($^{\circ}$)	30.00, 34.85, 38.87, 42.60, 45.00, 49.50, 52.75, 55.92, 59.02, 62.08, 65.12, 68.15, 71.21, 75.00

Table 1. Parameter grids used for the generation of the `zijiRetRad` table model (both blackbody and reflection share the same parameter values).

`const*TBabs*zijiBB,`

where `const` accounts for cross-calibration differences between the two *NuSTAR* detectors (FPMA and FPMB), `TBabs` models interstellar absorption (Wilms et al. 2000), and `zijiBB` is the blackbody table model generated with the `ziji` code. We fix the constant for FPMA to 1.0 and leave the corresponding one for FPMB as a free parameter. The same approach will later be applied when fitting with `relxillNS` (see Section 3.3).

The performance of the initial model is shown in the top panel of Fig. 4, where we plot the ratio between data and model. Several features remain unresolved: reflection signatures appear above 7 keV, with a sharp rise beyond 10 keV likely due to the

onset of the Compton hump, which a pure blackbody model cannot capture. To address this, we added our reflection table model (`zijiRefl`), leading to:

`const*TBabs*zijiRetRad,`

where `zijiRetRad` is the combined reflection and blackbody model. The ratio for this fit is shown in the middle panel of Fig. 4. The agreement improves substantially, with most reflection features accounted for. However, clear absorption residuals remain between 6–7 keV, corresponding to disk-wind features previously identified as Fe XXV and Fe XXVI absorption lines at 6.697 keV and 6.966 keV, respectively (Bianchi et al.

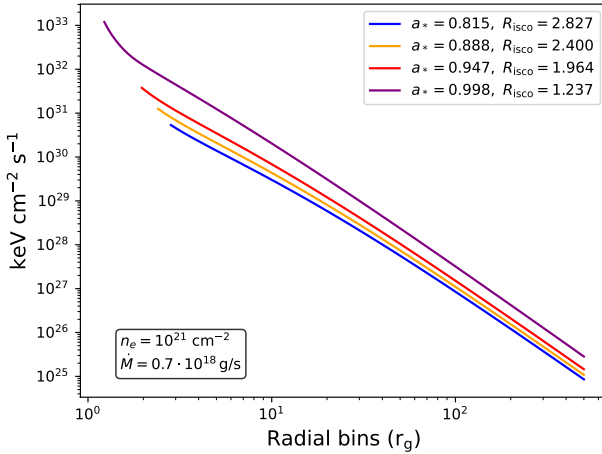


Fig. 3. Returning radiation flux profile in the rest frame of the disk for a $10 M_{\odot}$ black hole and for different values of the spin parameter.

2005; King et al. 2013; Pahari et al. 2018). To model them, we use a custom photoionization table generated with `xstar` (Kallman & Bautista 2001; Das et al. 2025), yielding the model:

```
const*TBabs*xstar*zijiRetRad.
```

This fit (Fig. 4, bottom panel) shows no major systematic deviations in the ratio plot, with a reduced χ^2 of 1.07. The model shown here represents the best-fit obtained with `zijiRetRad`, and the corresponding parameters are listed in Table 2 (3rd column). To determine the best-fit values and associated uncertainties, we ran `steppar` on each parameter, followed by `error` to estimate confidence intervals at the 90% level.

3.2. Results and Discussion

We report a rapidly spinning black hole ($a_* \sim 0.99$) and a disk inclination of $i \sim 53^\circ$. The hydrogen column density is estimated to be $N_{\text{H}} \sim 1.3 \cdot 10^{23} \text{ cm}^{-2}$, while the mass accretion rate is $\dot{M}_{\text{BH}} \sim 0.83 \cdot 10^{18} \text{ g/s}$, corresponding to approximately 15% \dot{M}_{Edd} . Moreover, we infer a high electron density of $n_e \sim 10^{21} \text{ cm}^{-3}$. Finally, the distance to the source inferred from our analysis is $D \sim 8.2 \text{ kpc}$.

The parameter values obtained in our analysis are generally consistent with those reported in the literature. Kuulkers et al. (1998), Connors et al. (2021), Das et al. (2025), and Tomsick et al. (1998) all reported high hydrogen column densities along the line of sight, with $N_{\text{H}} \sim (4 - 12) \cdot 10^{22} \text{ cm}^{-2}$. Gatuzz et al. (2019) reported a value closer to 10^{23} cm^{-2} , while Connors et al. (2021) adopted $N_{\text{H}} \sim 1.4 \cdot 10^{23} \text{ cm}^{-2}$, similar to our result. They justified this choice by pointing to the uncertainties in N_{H} derived from X-ray data (Tomsick et al. 1998; Tomsick & Kaaret 2000; Gatuzz et al. 2019), as well as the presence of dust scattering along the line of sight (Kalemci et al. 2018). The mass accretion rate is consistent with the value reported by Das et al. (2025) ($\dot{M}_{\text{BH}} \sim (15 - 20)\% \dot{M}_{\text{Edd}}$).

A high inclination has been reported by Tomsick et al. (1998), Seifina et al. (2014), and Connors et al. (2021), with values in the range $60^\circ < i < 70^\circ$. However, Connors et al. (2021) also found a lower estimate of $i \sim 37^\circ$ using `relxillNS`. Reflection modeling by King et al. (2014) provided an estimate of $i \sim 64^\circ$. Recent analyses by Draghis et al. (2024) and Das et al. (2025) reported somewhat lower inclination values of $i \sim 55^\circ$,

with the former exhibiting larger uncertainties; these values are closer to the one obtained in our analysis. The spin of the black hole has also been estimated to be high. King et al. (2014) found $a_* = 0.985^{+0.005}_{-0.014}$, and Connors et al. (2021) reported a similar value, although lower estimates have also appeared in the literature, e.g. $a_* = 0.857^{+0.095}_{-0.211}$ (Draghis et al. 2024), $0.85^{+0.07}_{-0.07}$ (Connors et al. 2021), and $0.837^{+0.067}_{-0.156}$ (Das et al. 2025).

The high electron density we find in our analysis is consistent with the results of Connors et al. (2021), who reported $n_e > 10^{20} \text{ cm}^{-3}$ across all spectral states. As discussed earlier (see Fig. 2(c)), such high densities are required for the reflection features to be present. In addition, the parameters we obtain for the `xstar` model are in good agreement with those reported by Das et al. (2025), analyzing the same observation.

The distance inferred in our analysis is lower than the values reported by Kalemci et al. (2025) and Kalemci et al. (2018) ($\sim 11.5 \text{ kpc}$) when modeling the dust-scattering halo, as well as the 10 kpc distance commonly adopted in the literature (see, e.g., Seifina et al. 2014; Augusteijn et al. 2001). To provide a direct comparison, we repeat our analysis using the same spectral model but fixing the distance to 10 kpc, and refit the data. The best-fit parameter values for this configuration are reported in the last column of Table 2. As in our baseline fit, the solution favors a rapidly rotating black hole; however, the inclination angle is lower and the inferred mass accretion rate is higher. We do not discuss all parameter changes in detail, as this is beyond the scope of the present work, but we note that the shifts are consistent with the parameter correlations revealed by the MCMC analysis (see Fig. A.1). The corresponding model components and residuals are shown in the middle panel of Fig. 5. In this case, the residuals display a clear increasing trend at high energies, indicating that the model struggles to reproduce the observed high-energy tail.

3.3. Comparison with `relxillNS`

To place our results in context, we compare `zijiRetRad` with `relxillNS` (García et al. 2022), a model widely applied for returning radiation (Connors et al. 2020; Connors et al. 2021). It is worth noting that `relxillNS` is not a true self-irradiation model: instead of using the intrinsic disk spectrum, it illuminates the accretion disk with a single-temperature blackbody. While `zijiRetRad` relies on the well-tested `reflionx` (Ross & Fabian 2005) radiative transfer code, `relxillNS` uses `xillverNS` (García et al. 2022). Since `relxillNS` has been extensively studied in the literature, we do not present its setup in detail here. We fit the same observational data with `relxillNS`, and the resulting best-fit model is:

```
const*TBabs*xstar*(nthComp+kerrbb+relxillNS),
```

where `nthComp` accounts for the Comptonized emission (assuming a multicolor disk blackbody seed spectrum; `inp_type = 1`) and `kerrbb` for the multicolor blackbody. We fix the power-law index, $\Gamma = 2.5$, and the electron temperature, $kT_e = 100 \text{ keV}$, of `nthComp`, leaving only the normalization as a free parameter. Moreover, the distance is fixed at $D = 10 \text{ kpc}$ (Seifina et al. 2014; Augusteijn et al. 2001), since it cannot be simultaneously constrained with the mass accretion rate within this model. The mass is fixed at $10 M_{\odot}$ (Seifina et al. 2014) and the iron abundance at the solar value ($A_{\text{Fe}} = 1$), ensuring consistency with the prior analysis using `zijiRetRad`. For reference, `zijiBB` and `kerrbb` are essentially equivalent.

The best-fit values obtained with `relxillNS` are listed in Table 3. They are broadly consistent with earlier studies and

Component	Parameter	Model 1	Model 2
TBabs	$N_{\text{H}} (10^{22} \text{ cm}^{-2})$	$13.35^{+0.18}_{-0.23}$	$13.60^{+0.15}_{-0.18}$
xstar	$column (10^{23})$	$1.10^{+0.16}_{-0.13}$	$1.01^{+0.12}_{-0.07}$
	$rlog\xi$	$4.01^{+0.10}_{-0.09}$	$3.95^{+0.09}_{-0.05}$
zijiRetRad	$n_{\text{e}} (10^{21} \text{ cm}^{-3})$	$1.00^{+1.33}_{-0.34}$	$0.101^{+0.076}_{-0.004}$
	a_{*}	$0.9878^{+0.0002}_{-0.0003}$	$0.98653^{+0.00006}_{-0.00008}$
	$M_{\text{BH}} (\text{M}_{\odot})$	10^{*}	10^{*}
	$\dot{M}_{\text{BH}} (10^{18} \text{ g/s})$	$0.83^{+0.04}_{-0.08}$	$1.235^{+0.007}_{-0.008}$
	$i (\text{)}^{\circ}$	$52.6^{+0.4}_{-0.7}$	$46.6^{+0.2}_{-0.3}$
	$D (\text{kpc})$	$8.19^{+0.16}_{-0.43}$	10^{*}
constant	C_{FPMA}	$0.987^{+0.002}_{-0.002}$	$0.987^{+0.002}_{-0.002}$
	χ^2/ν	$766.71/718 = 1.07$	$803.05/719 = 1.12$

Table 2. Best-fit values obtained using `zijiRetRad`. The asterisk (*) denotes that the parameter is fixed at this value.

with the results from `zijiRetRad`, although some differences are worth highlighting. In particular, `relxillNS` returns lower electron density and accretion rate. We obtain $\dot{M}_{\text{BH}} \sim 0.58 \cdot 10^{18} \text{ g/sec}$, corresponding to $\sim 13\% M_{\text{Edd}}$. The electron density lies between $\sim 10^{15} - 10^{18} \text{ cm}^{-3}$, whereas `zijiRetRad` requires densities around 10^{21} cm^{-3} . A detailed examination of all parameter values is beyond the scope of this study.

The model components and residuals are shown in Fig. 5, where the left and middle panels correspond to `zijiRetRad` and the right panels correspond to `relxillNS`. The most notable difference between the two models is that the `zijiRetRad` reflection spectrum is significantly harder at high energies relative to `relxillNS`. Consequently, only the latter one requires an additional weak coronal component to produce the observed high-energy tail. In the case of `zijiRetRad`, the hard excess arises naturally from the iterative reflection included in the model, which is absent in `relxillNS`. Fig. 6 shows the relativistic reflection spectra for different numbers of iterations (0–3) and for varying black hole spins. The high-energy tail becomes progressively harder with increasing iteration number and black hole spin. As the disk (R_{isco}) moves closer to the black hole, gravitational light bending and Doppler blueshift increase the flux reaching the disk from its innermost regions, resulting in a harder high-energy spectrum for the iterative reflection. Interestingly, without accounting for a coronal component, producing a high-energy tail in the reflection spectrum requires pushing the spin parameter to high values. As a result, neglecting the corona could lead to overestimating the inferred spin in some cases, when such tails are present in the data. However, in our case, we verified that including a coronal component alongside `zijiRetRad` does not improve the quality of the fit.

4. Concluding Remarks and Future Work

This study presents an XSPEC table model that isolates the reflection spectrum produced by returning radiation from the accretion disk, excluding any contribution from the corona. When applied to the black hole XRB 4U 1630–47 in the soft state, the model provides a good fit to the data ($\chi^2/\nu = 1.07$). The best-fit indicates a high black hole spin ($a_{*} \sim 0.99$), a disk inclination of $i \sim 53^{\circ}$, an increased electron density ($n_{\text{e}} \sim 10^{21} \text{ cm}^{-3}$) and a mass accretion rate of $\dot{M}_{\text{BH}} \sim 15\% M_{\text{Edd}}$, broadly consistent

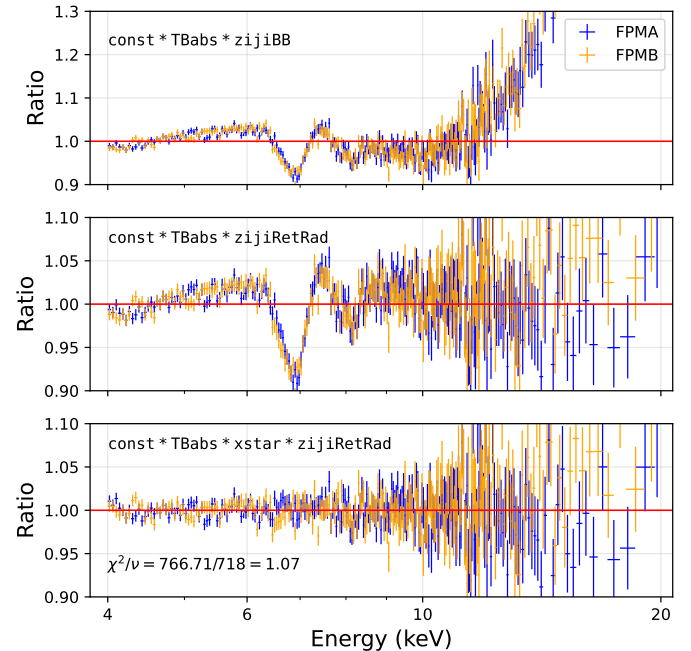


Fig. 4. Ratio plots for the different models utilized during model build-up using `zijiRetRad`. The respective models are shown in the upper part of each panel. The lower panel shows the best-fit model alongside the reduced χ^2 obtained. Blue and orange colors correspond to FPMA and FPMB respectively.

with previous studies. The inferred source distance, $D \sim 8.2 \text{ kpc}$, is lower than the $\sim 10 \text{ kpc}$ value commonly adopted in the literature, indicating a modest difference relative to earlier estimates.

We compared our model with the widely used `relxillNS`. Our analysis shows that `relxillNS` requires a weak corona to adequately describe the data, in contrast to `zijiRetRad`. The latter produces a harder reflection spectrum at high energies and can naturally produce the high-energy tail without needing an additional Comptonized component. This behavior arises from the iterative reflection implemented in the `ziji` code, as well as from the high spin value inferred by our model (see Fig. 6).

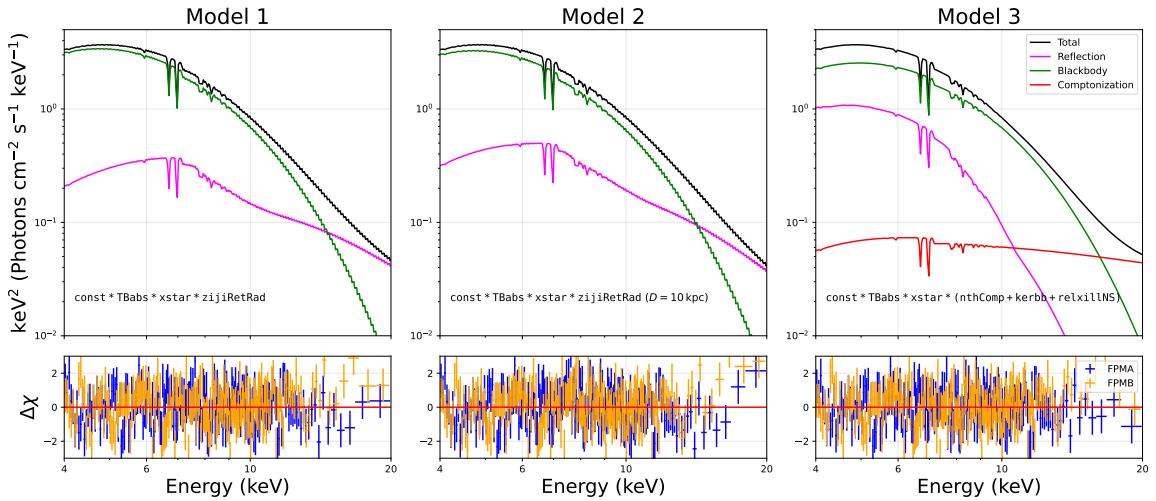


Fig. 5. Model components (upper panels) and $\Delta\chi = (\text{data} - \text{model})/\text{error}$ (lower panels) for the best-fit models obtained with `zijiRetRad` (left panels with D free and middle panels with $D = 10$ kpc) and with `relxillNS` (right panels). The green, magenta, red, and black curves correspond to the blackbody, reflection, Comptonization, and total spectra, respectively. In the upper left and middle (right) panels, the reflection and blackbody components correspond to `zijiRefl` (`relxillNS`) and `zijiBB` (`kerbb`), while the Comptonization component (`nthComp`) is present only in the `relxillNS` panel. The total model is indicated at the bottom of each upper panel.

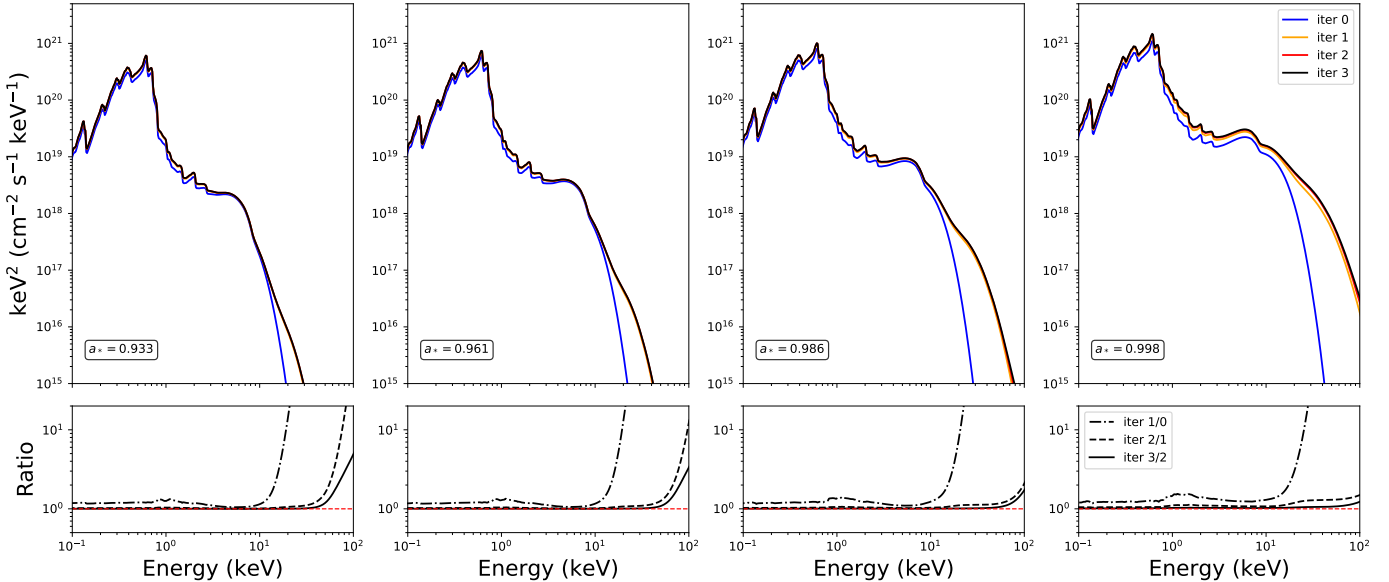


Fig. 6. Relativistic reflection spectra generated with the `ziji` code for different numbers of iterative reflections (0–3) and spin values (upper panels). The bottom panels show the ratio between the flux of each successive iteration. Model parameters were randomly selected to illustrate the qualitative behaviour of the spectrum as the number of iterations increase (in all panels: $M_{\text{BH}} = 10 M_{\odot}$, $\dot{M}_{\text{BH}} = 0.3 \cdot 10^{18} \text{ g/s}$, $n_{\text{e}} = 10^{22} \text{ cm}^{-3}$, $i = 45^\circ$). Iteration 0 represents the reflection spectra produced solely by the direct returning radiation of the thermal component, while iterations 1–3 show the reflection spectra that also include the returning radiation of the reflection component for the corresponding number of iterations.

Our model is, of course, a simplification, as we neglect the corona entirely, even though it is thought to be weak or even absent in soft states. Nevertheless, the results demonstrate that returning radiation alone can account for the observed spectra and should therefore be considered an important component during the high-soft state. A natural next step is to include a weak corona self-consistently, in order to assess the relative contributions of coronal emission and self-irradiation. Extending the parameter grid of our model would also be valuable, particularly by including lower spin and mass values. Yet, as previously discussed, slower rotation would reduce the impact of return-

ing radiation. Finally, to further generalize these findings, it will also be necessary to apply this approach to additional sources in the soft state and eventually make the model publicly available within the XSPEC community, which will be the subject of a forthcoming paper.

Component	Parameter	Model 3
TBabs	N_{H} (10^{22} cm^{-2})	$12.3^{+0.3}_{-0.5}$
xstar	$column$ (10^{23})	$1.07^{+0.17}_{-0.14}$
	$rlog\xi$	$4.01^{+0.10}_{-0.10}$
nthComp	$Gamma$	2.5^*
	kT_{e} (keV)	100^*
	$norm$ (10^{-2})	$4.84^{+0.17}_{-0.16}$
kerrbb	a_*	$0.998^{+0.005}_{-0.005}$
	i ($^{\circ}$)	$56.15^{+1.05}_{-1.08}$
	\dot{M}_{BH} (10^{18} g/s)	$0.58^{+0.04}_{-0.05}$
	M_{BH} (M_{\odot})	10^*
	D (kpc)	10^*
relxillNS	kT_{bb} (keV)	$0.89^{+0.03}_{-0.03}$
	$log\xi$	$2.46^{+0.21}_{-0.25}$
	$log(n_{\text{e}})$ (cm^{-3})	$17.5^{+0.7}_{-0.7}$
	A_{Fe}	1.0^*
	$norm$ (10^{-2})	$1.9^{+0.6}_{-0.4}$
constant	C_{FPMA}	$0.987^{+0.002}_{-0.002}$
	χ^2/ν	$758.26/715 = 1.06$

Table 3. Same as Table 2, but for relxillNS. The superscript (subscript) p indicates that the parameter is constrained at the maximum (minimum) value permitted by the model.

Appendix A: MCMC Analysis for *zijiRetRad*

To characterize the posterior distributions of the best-fit parameters listed in Table 2, we employed the Markov Chain Monte Carlo (MCMC) implementation in XSPEC, which uses the affine-invariant ensemble sampler of [Goodman & Weare \(2010\)](#). We initialized 50 walkers and evolved the chains for 10,000,000 steps, discarding the first 100,000 steps as burn-in. The corner plot for the best fit model parameters listed in Table 2 is shown in Fig. A.1.

We find several strong parameter correlations in the MCMC posterior. There is strong correlation between the two parameters of the *xstar* model; column density and ionization parameter. Physically, a higher ionization corresponds to a larger fraction of fully stripped iron and therefore a higher column density is required to produce the same absorption line. In the *zijiRetRad* model, the mass accretion rate and the source distance are also strongly correlated, since both primarily act as scaling factors for the observed flux, see Fig. 2(b). The inclination is correlated with both the mass accretion rate and the distance, while the black hole spin is correlated with the inclination and the accretion rate. Higher spin decreases R_{isco} , increasing the inner disk flux, so that the same observed flux can be reproduced with a lower mass accretion rate (roughly, $F \propto \dot{M}_{\text{BH}}/R_{\text{isco}}^2$). Changes in inclination affect both the observed flux and the spectral shape, so the apparent anti-correlations involving the inclination result from the interplay of spin, distance, and accretion rate to recover the observed flux. These correlations reflect intrinsic degeneracies in a flux-calibrated model without a free normalization and do not affect our main conclusions.

Appendix B: Distance Estimation

The source distance can be inferred from the model normalization through the flux-luminosity relation:

$$F_{\text{table}} = \frac{L}{4\pi D_{\text{ref}}^2}, \quad F_{\text{obs}} = \frac{L}{4\pi D_{\text{source}}^2}, \quad (\text{B.1})$$

and therefore:

$$F_{\text{obs}} = \left(\frac{D_{\text{ref}}}{D_{\text{source}}} \right)^2 F_{\text{table}}. \quad (\text{B.2})$$

Here, F_{table} is the flux at the reference distance $D_{\text{table}} = 10^6 r_g$ ($r_g = GM/c^2$) used in the table model and F_{obs} is the flux at the true source distance D_{source} . Thus, the model's normalization plays the role of the geometric prefactor:

$$\mathcal{N} = (D_{\text{ref}}/D_{\text{source}})^2, \quad (\text{B.3})$$

so that $F_{\text{obs}} = \mathcal{N} F_{\text{table}}$. We derive the following relation, which directly connects the model's normalization to the physical distance:

$$\mathcal{N} = 0.229 \cdot 10^{-20} \frac{M^2 (\text{M}_\odot)}{D^2 (\text{kpc})}. \quad (\text{B.4})$$

We note that the factor of 10^{-20} is absorbed into the calculated flux of the table model. Consequently, the normalization should be evaluated without this factor when using the model.

Acknowledgements

K.K. would like to thank Arthur Suvorov and Marta Piscitelli for carefully reading the manuscript and providing valuable feedback. K.K. also acknowledges José Olvera Meneses for helpful discussions on accretion disk physics.

References

Abbott, B. P., Abbott, R., Abbott, T. D., et al. 2016, Phys. Rev. Lett., 116, 061102
 Abbott, B. P., Abbott, R., Abbott, T. D., et al. 2019, Physical Review X, 9, 031040
 Abdikamalov, A. B., Ayzenberg, D., Bambi, C., et al. 2020, ApJ, 899, 80
 Arnaud, K. A. 1996, in ASP Conf. Ser., Vol. 101, Astronomical Data Analysis Software and Systems V, ed. G. H. Jacoby & J. Barnes, 17
 Augusteijn, T., Kuulkers, E., & van Kerwijk, M. H. 2001, A&A, 375, 447
 Bambi, C. 2017, Black Holes: A Laboratory for Testing Strong Gravity (Springer)
 Bambi, C. 2024a, arXiv, 2408.12262
 Bambi, C. 2024b, Testing Gravity with Black Hole X-Ray Data (Singapore: Springer Nature Singapore), 149–182
 Bambi, C., Brenneman, L. W., Dauser, T., et al. 2021, Space Sci. Rev., 217, 65
 Bianchi, S., Matt, G., Nicastro, F., Porquet, D., & Dubau, J. 2005, MNRAS, 357, 599
 Blandford, R. D. & Znajek, R. L. 1977, MNRAS, 179, 433
 Connors, R. M. T., García, J. A., Dauser, T., et al. 2020, ApJ, 892, 47
 Connors, R. M. T., García, J. A., Tomsick, J., et al. 2021, ApJ, 909, 146
 Cunningham, C. 1976, ApJ, 208, 534
 Dabrowski, Y., Fabian, A. C., Iwasawa, K., Lasenby, A. N., & Reynolds, C. S. 1997, MNRAS, 288, L11
 Das, D., Liu, H., Zhang, Z., et al. 2025, arXiv, 2509.09481
 Dauser, T., García, J., Wilms, J., et al. 2013, MNRAS, 430, 1694
 Dauser, T., García, J. A., Joyce, A., et al. 2022, MNRAS, 514, 3965
 Dauser, T., Wilms, J., Reynolds, C. S., & Brenneman, L. W. 2010, MNRAS, 409, 1534
 De Rosa, A., Uttley, P., Gou, L., et al. 2019, Sci. China Phys. Mech. Astron., 62, 29504
 Dovciak, M., Karas, V., & Yaqoob, T. 2004, ApJS, 153, 205
 Draghis, P. A., Miller, J. M., Costantini, E., et al. 2024, ApJ, 969, 40
 Fabian, A. C., Iwasawa, K., Reynolds, C. S., & Young, A. J. 2000, PASP, 112, 1145
 Fabian, A. C., Rees, M. J., Stella, L., & White, N. E. 1989, MNRAS, 238, 729
 Fabian, A. C., Wilkins, D. R., Miller, J. M., et al. 2012, MNRAS, 424, 217
 García, J., Dauser, T., Lohfink, A., et al. 2014, ApJ, 782, 76
 García, J., Dauser, T., Reynolds, C. S., et al. 2013, ApJ, 768, 146
 García, J. & Kallman, T. R. 2010, ApJ, 718, 695
 García, J. A., Dauser, T., Ludlam, R., et al. 2022, ApJ, 926, 13
 García, J. A., Steiner, J. F., McClintock, J. E., et al. 2015, ApJ, 813, 84
 Gatuzz, E., Díaz Trigo, M., Miller-Jones, J. C. A., & Migliari, S. 2019, MNRAS, 482, 2597
 George, I. M. & Fabian, A. C. 1991, MNRAS, 249, 352
 Goodman, J. & Weare, J. 2010, Commun. Appl. Math. Comput. Sci., 5, 65
 Huang, Y., Liu, H., Mirzaev, T., et al. 2025, ApJ, 989, 168
 Ingram, A., Mastroserio, G., Dauser, T., et al. 2019, MNRAS, 488, 324
 Ingram, A. R. & Motta, S. E. 2019, New A Rev., 85, 101524
 Jiang, J., Abdikamalov, A. B., Bambi, C., & Reynolds, C. S. 2022, MNRAS, 514, 3246
 Kalemci, E., Diaz Trigo, M., Oztaban, E., et al. 2025, MNRAS, 543, 3073
 Kalemci, E., Maccarone, T. J., & Tomsick, J. A. 2018, ApJ, 859, 88
 Kallman, T. & Bautista, M. 2001, ApJS, 133, 221
 Kerr, R. P. 1963, Phys. Rev. Lett., 11, 237
 King, A. L., Miller, J. M., Gültekin, K., et al. 2013, ApJ, 771, 84
 King, A. L., Walton, D. J., Miller, J. M., et al. 2014, ApJ Lett., 784, L2
 King, A. R. & Kolb, U. 1999, MNRAS, 305, 654
 Kuulkers, E., Wijnands, R., Belloni, T., et al. 1998, ApJ, 494, 753
 Laor, A. 1991, ApJ, 376, 90
 Li, L.-X., Zimmerman, E. R., Narayan, R., & McClintock, J. E. 2005, ApJS, 157, 335
 Li, S., Nosirov, A., Bambi, C., et al. 2025, arXiv e-prints, arXiv:2509.20752
 Lindquist, R. W. 1966, Ann. Phys., 37, 487
 Liu, H., Abdikamalov, A. B., Ayzenberg, D., et al. 2019, Phys. Rev. D, 99, 123007
 Liu, H., Abdikamalov, A. B., Mirzaev, T., et al. 2025, MNRAS, 536, 2594
 Liu, H., Bambi, C., Jiang, J., et al. 2023a, ApJ, 950, 5
 Liu, H., Ji, L., Bambi, C., et al. 2021, ApJ, 909, 63
 Liu, H., Jiang, J., Zhang, Z., et al. 2023b, ApJ, 951, 145
 Liu, H., Wang, H., Abdikamalov, A. B., Ayzenberg, D., & Bambi, C. 2020, ApJ, 896, 160

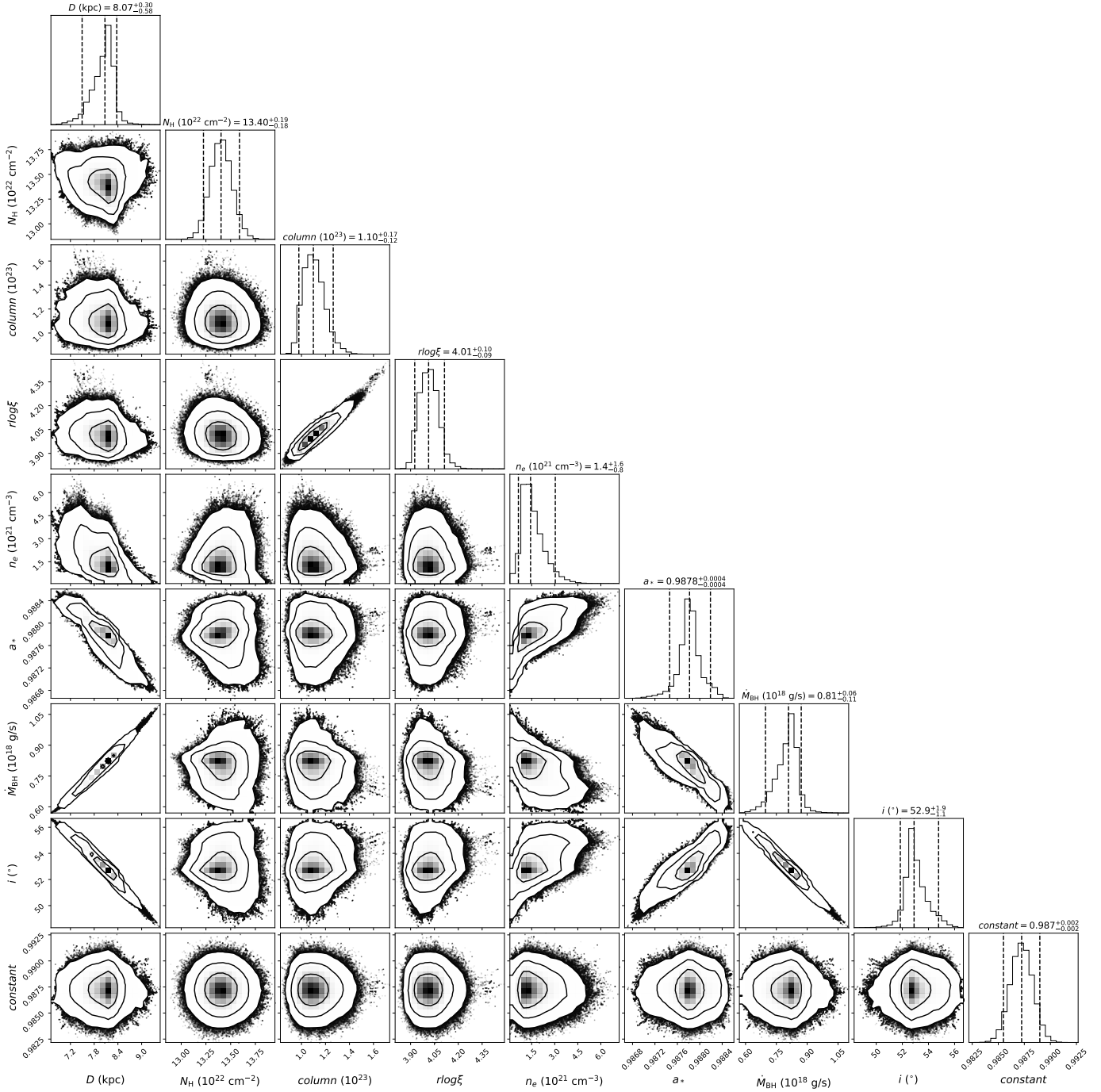


Fig. A.1. Corner plot for the best fit model using `zijiRetRad`. The error values of each of the parameter corresponds to 90% confidence level. The contours correspond to 68%, 95% and 97.5% confidence levels.

McClintock, J. E., Narayan, R., & Steiner, J. F. 2014, Space Science Reviews, 183, 295
 Miller, M. C. & Miller, J. M. 2015, Physics Reports, 548, 1, the masses and spins of neutron stars and stellar-mass black holes
 Mirzaev, T., Bambi, C., Abdikamalov, A. B., et al. 2024a, ApJ, 976, 229
 Mirzaev, T., Riaz, S., Abdikamalov, A. B., et al. 2024b, ApJ, 965, 66
 Motta, S. E., Belloni, T. M., Stella, L., Muñoz-Darias, T., & Fender, R. 2014a, MNRAS, 437, 2554
 Motta, S. E., Munoz-Darias, T., Sanna, A., et al. 2014b, MNRAS, 439, L65
 Niedzwiecki, A., Szanecki, M., & Zdziarski, A. A. 2019, MNRAS, 485, 2942
 Niedzwiecki, A. & Zdziarski, A. A. 2018, MNRAS, 477, 4269
 Niedzwiecki, A., Zdziarski, A. A., & Szanecki, M. 2016, ApJ Lett., 821, L1
 Niedzwiecki, A. & Zycki, P. T. 2008, MNRAS, 386, 759
 Novikov, I. D. & Thorne, K. S. 1973, in Black Holes (Les Astres Occlus), ed. C. Dewitt & B. S. Dewitt, 343–450
 Page, D. N. & Thorne, K. S. 1974, ApJ, 191, 499
 Pahari, M., Bhattacharyya, S., Rao, A. R., et al. 2018, ApJ, 867, 86
 Penrose, R. 1969, Nuovo Cimento Rivista Serie, 1, 252
 Reynolds, C. S. 2014, Space Sci. Rev., 183, 277
 Reynolds, C. S. 2021, ARA&A, 59, 117
 Riaz, S., Ayzenberg, D., Bambi, C., & Nampalliwar, S. 2020a, ApJ, 895, 61
 Riaz, S., Ayzenberg, D., Bambi, C., & Nampalliwar, S. 2020b, MNRAS, 491, 417
 Riaz, S., Mirzaev, T., Abdikamalov, A. B., & Bambi, C. 2023, Eur. Phys. J. C, 83, 838
 Riaz, S., Szanecki, M., Niedzwiecki, A., Ayzenberg, D., & Bambi, C. 2021, ApJ, 910, 49
 Ross, R. R. & Fabian, A. C. 2005, MNRAS, 358, 211
 Schnittman, J. D. & Krolik, J. H. 2009, ApJ, 701, 1175
 Seifina, E., Titarchuk, L., & Shaposhnikov, N. 2014, ApJ, 789, 57

Shakura, N. I. & Sunyaev, R. A. 1973, A&A, 24, 337
Shapiro, S. L., Lightman, A. P., & Eardley, D. M. 1976, ApJ, 204, 187
Shashank, S., Riaz, S., Abdikamalov, A. B., & Bambi, C. 2022, ApJ, 938, 53
Thorne, K. S. & Price, R. H. 1975, ApJ, 195, L101
Tomsick, J. A. & Kaaret, P. 2000, ApJ, 537, 448
Tomsick, J. A., Lapshov, I., & Kaaret, P. 1998, ApJ, 494, 747
Tripathi, A., Abdikamalov, A. B., Ayzenberg, D., Bambi, C., & Liu, H. 2021a, ApJ, 913, 129
Tripathi, A., Nampalliwar, S., Abdikamalov, A. B., et al. 2019, ApJ, 875, 56
Tripathi, A., Zhang, Y., Abdikamalov, A. B., et al. 2021b, ApJ, 913, 79
Tripathi, A., Zhou, B., Abdikamalov, A. B., et al. 2020, Phys. Rev. D, 102, 103009
Walton, D. J., Tomsick, J. A., Madsen, K. K., et al. 2016, ApJ, 826, 87
Wilkins, D. R., Garcia, J. A., Dauser, T., & Fabian, A. C. 2020, MNRAS, 498, 3302
Wilms, J., Allen, A., & McCray, R. 2000, ApJ, 542, 914
Zhang, S. N., Cui, W., & Chen, W. 1997, ApJ, 482, L155